Why tDCS models cannot be trusted yet? — A simulation study

Martin Grignard [*], Christophe Geuzaine [†], Michel Hansenne [‡], Steve Majerus [‡§], Christophe Phillips [*§]

January 3, 2023

Abstract

Transcranial direct current stimulation (tDCS) has gained increased interest over the past decades due to its affordability, ease of use and wide range of applications. However, its lack of consistency and reproducibility of published results is rising concerns.

A potential solution to improve the method is to tailor the stimulation for each subject based on individual measurements and models. Such model requires accurate information about the geometry of the tissues composing the head of the subjects, about their electric properties and about the electrode montage.

In the present simulation work, we evaluate the effect of an error on the placement of the anode and of the unknown physical properties of the tissues on the induced electric field for 6 experiments on 20 subjects.

In addition to confirming the concerning small tDCS effect size, we show that the uncertainty on the conductivity parameters prevents any other conclusion to be drawn from such models.

1 Introduction

Transcranial direct current stimulation (tDCS) is a non-invasive neuromodulation technique which consists in injecting a small amount of electric current (*i.e.*, usually 1 to 2 mA) through the head of a subject by the mean of two large saline-soaked sponge electrodes (*e.g.*, 5×5 cm^2). The stimulating electrode or anode is placed above the cortical region of interest. The reference electrode, also referred to as cathode, is either located on the same region of the opposite hemisphere in a bipolar electrode montage or on the contralateral orbit region in a unipolar montage. It can also be applied on a silent zone such as the chin, the neck or the deltoid muscle [28, 36].

Since the beginning of the century, this tool has received increased interest due to its affordability, simplicity and wide range of application. Indeed, it has been studied in research and clinical applications to help patients recovering from strokes [5], traumatic spinal cord injury [30] or suffering from refractory epilepsy [62], fibromyalgia [31], depression [45], anxiety disorders [53] just to name a few. A lot of studies have also tried to use tDCS to improve cognitive functions like working memory or inhibition in normal subjects and patients [11, 50, 52].

Whilst more and more papers focusing on tDCS are published every year (1,088 papers listed on PubMed in 2021[1]), two major issues rose up: the high inter-subject variability in the response to the stimulation and the lack of reproducibility of some published results in follow-up studies [12, 24, 59].

With a percentage of expected response generally lower than 50 % [23, 35], the reliability of tDCS is questionable. Wiethoff et al. [60] concludes that the after-effect of tDCS on corticospinal excitability is highly variable, and the systematic review of Horvath et al. [22] rose questions about the efficacy of such device and the underlying mechanisms.

One of the proposed solutions to improve the technique is to individualize the intensity of the injected current, referred to as the dose, based on subject specific models [1]. Unfortunately, the recent work by Sallard et al. [48] indicates that this approach might not improve the efficacy of tDCS over the primary motor cortex. Nevertheless, current modelling is often performed in addition to tDCS to evaluate the current density induced by the stimulation in a given region of interest (ROI).

Such a model relies heavily on the geometry of the subject and on the electrode placement, but also on the electric properties of the tissues composing the head. Those properties have been shown to vary widely between subjects based on numerous factors (*e.g.*, temperature, time of day, health status...). The review from [33] provides ranges of low frequency conductivity values for the main biological tissue classes.

The head geometry is usually built based on subject-specific structural images, but electrode positions are not always recorded using virtualization techniques. In this case, they are placed on the model without real world information, inducing a potential error of placement.

On the other hand, the physical properties of the tissues are hard to measure on a subject basis. Hence, constant values across subjects are usually set according to the lit-

*. M. Grignard and C. Phillips (Corresponding author) are with the GIGA CRC In-Vivo Imaging, University of Liège, Liège, Belgium (e-mail: mar.grignard@uliege.be, c.phillips@uliege.be)

†. C. Geuzaine is with the Department of Electrical Engineering and Computer Science, University of Liège, Liège, Belgium

‡. M. Hansenne and S. Majerus are with the Psychology & Neuroscience of Cognition (PsyNCog) research unit, University of Liège, Liège, Belgium

§. S. Majerus and C. Phillips are with the Belgian Fund for Scientific Research (FRS-FNRS)

1. `https://pubmed.ncbi.nlm.nih.gov/?term=tDCS&filter=years.2021-2021`

erature.

In the present simulation work, we study the electric field induced in four different ROIs of the left hemisphere by the injection of 2 mA with six electrode montages (See Table 1) and compute the induced transmembrane potential (ITP) on the 20 subjects from BrainWeb[2]. Previous studies reported ITP values between 0.2 and 0.5 mV [37, 42].

Anode	Cathode	ROI	Bipolar	Unipolar
C3	C4	MC	■	□
C3	Fp2		□	■
F3	F4	dlPFC	■	□
F3	Fp2		□	■
F7	F8	vmPFC	■	□
P3	P4	IPS	■	□

Tab. 1 The electrode montages considered with the ROI they target.

In the process, we account for an error of 1 cm on the anode placement in four directions relative to the reference EEG 10-20 position and for the uncertainty on the electric conductivity of the biological tissues.

2 Materials and methods

2.1 Dataset

We used the dataset of 20 simulated normal healthy adults (10 females and 10 males) made available by BrainWeb. For each subject, this dataset provides a structural T1-weighted generated based on a SFLASH sequence (TR=22 ms, TE=9.2 ms, flip angle=30° and 1 mm isotropic voxel size), 12 fuzzy tissue probability maps and a discrete segmented volume [2, 3].

In the present work, only the T1-weighted images and discrete models were first converted into NIfTI images using *Nibabel* [6] and sorted following BIDS specifications [16] to be further processed.

2.2 Head geometry

To simulate the electric current in the head of the subjects, we generated finite element models based on the labelled images. These original segmented volumes with $0.5 \times 0.5 \times 0.5$ mm^3 voxels were first cleaned to remove external objects and noise (See Figure 1a and Figures S1-20a) in four consecutive steps.

First, we created manually binary masks using *itk-SNAP* [63] to remove big objects adjacent to the scalp from subjects 18 and 42. The other subjects did not require such manual processing. After this step, an iterative binary opening was performed on the whole head masks until no change between two iterations was measured. This removed the small external clusters. To erase the remaining non-head bodies, we kept only the biggest remaining cluster using *Scipy* [57]. Finally, we enforced at least one layer of CSF around the gray matter and one layer of soft tissues around the skull.

Next, we merged the original 11 tissues (referred to as SEG-11) into 5 tissues (SEG-05). Indeed, the most common models used to simulate tDCS include only five main tissues classes, namely: white matter (WM), gray matter (GM), cerebrospinal fluid (CSF), skull (SKL) and soft tissues (SFT). This can be attributed to the fact that most of the available automated head segmentation pipelines only output these tissues, even though a recent effort in the community has led to the release of several tools that can produce more accurate models [40, 54].

The merging rules are described in Table S1 from the supplementary materials, and the resulting labels are presented in Figure 1b for subject 41 (See Figures S1-20b for the other subjects).

These final labels were processed with Shamo [17] to generate subject specific finite element models (FEM). The obtained models contained more than 2×10^6 tetrahedra (See Figure 1c and Figures S1-20c).

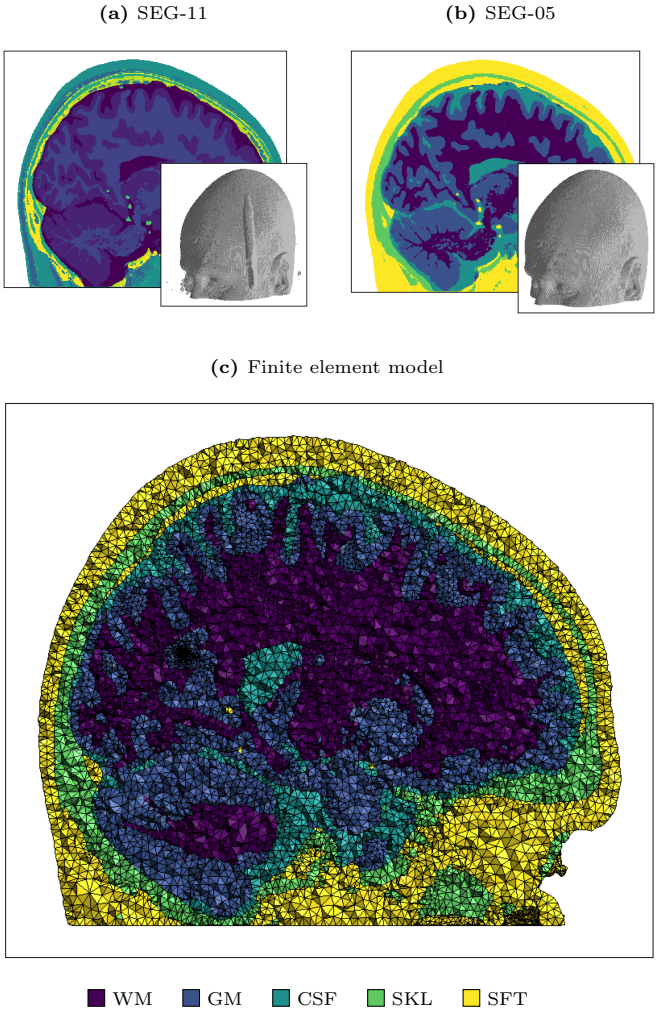

Fig. 1 (a) The original SEG-11 model, **(b)** the SEG-05 obtained by first cleaning the labels and then merging tissues following the rules defined in Table S1 and **(c)** a sagittal cut of the resulting FEM for subject 41.

2.3 Electrode placement

Since one of the goals of this study is to evaluate the effect of the error on the placement of the electrodes, we considered five different positions of the anode for each of the experiments from Table 1 where the electrode was moved by 1 cm relative to the reference EEG 10-20 international system [25, 27] position.

2. `https://brainweb.bic.mni.mcgill.ca/`

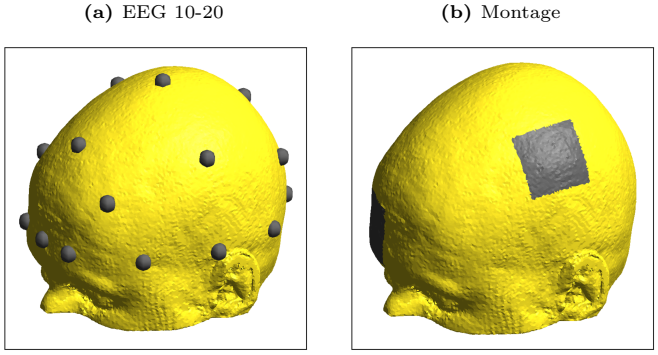

(a) EEG 10-20 **(b)** Montage

Fig. 2 (a) The automatically computed EEG 10-20 electrode positions and **(b)** the resulting model for the C3-Fp2 electrode montage on subject 41.

We denote the four perturbation directions as central (C)/lateral (L) if the electrode moves toward/away from the symmetry axis of the head and anterior (A)/posterior (P) if the electrode moves towards the front/back of the head. The name of the displaced anode is the concatenation of its base name and the direction (*e.g.*, central P3 is referred to as P3C).

The BrainWeb dataset does not include electrode positions. Consequently, we first located the nasion (NZ), the inion (IZ) and the left and right helix-tragus junction (LHJ and RHJ) in RAS coordinate system manually using *MRIcron* [47]. Then, we generated a high density mesh of the head surface using Shamo [17] and implemented the procedure proposed by Jurcak et al. [26] to compute the coordinates of both the reference electrodes and their displaced counterparts (See Figure 2a and Figures S1-20d).

We then produced a finite element model for each electrode montage with each position of the anode by adding the sensors to the base mesh from Section 2.2. The electrodes were modelled as 5×5 cm^2 square patches, as shown in Figure 2b for the C3-Fp2 electrode montage on subject 41 (See Figures S1-20e-j for the other montages and subjects). This step resulted in the creation of 30 models per subject (600 models in total).

2.4 Electrical conductivity

In our previous work [17], we showed that the electrical conductivity of the tissues κ (S m^{-1}) influences the results of the simulations by using the conductivity values reported by McCann et al. [33] (See Table 2). The mean values in the table are the reported weighted means computed using a weighting method described in their paper. We used the same values in the present study.

Tissue	Electrical conductivity (S m^{-1})			
	Min.	Max.	Mean	Std.
WM	0.0646	0.8100	0.2167	0.1703
GM	0.0600	2.4700	0.4660	0.2392
CSF	1.0000	2.5100	1.7100	0.2981
SKL	0.0182	1.7180	0.0160	0.0190
SFT	0.1370	2.1000	0.4137	0.1760

Tab. 2 The electrical conductivities of the tissues (S m^{-1}) as reported by McCann et al. [33].

The electrical conductivity considered for the soft tissues class (SFT) was set as the one measured for the scalp since its range encompasses those of fat, muscle, and blood which are the three main classes that were merged into it.

We defined 20 different conductivity profiles $\boldsymbol{\kappa} = [\kappa_{\mathrm{WM}}, \kappa_{\mathrm{GM}}, \kappa_{\mathrm{CSF}}, \kappa_{\mathrm{SKL}}, \kappa_{\mathrm{SFT}}]$ by sampling the 5D uniform conductivity space with a quasi-random Halton sequence [19] (See Table S2a in supplementary material). This space, $\Omega_{\mathrm{uniform}}$, was defined by five uniform distributions ranging from the minimum to the maximum conductivity value for each tissue.

In addition to these profiles, we also determined the reference conductivity profile, as recommended by McCann et al. [33] (*i.e.* $\boldsymbol{\kappa} = [\bar{\kappa}_{\mathrm{WM}}, \bar{\kappa}_{\mathrm{GM}}, \bar{\kappa}_{\mathrm{CSF}}, \bar{\kappa}_{\mathrm{SKL}}, \bar{\kappa}_{\mathrm{SFT}}]$).

The uniform distributions used to define $\Omega_{\mathrm{uniform}}$ are considered as the worst case scenario, since some ranges reported by McCann et al. span multiple orders of magnitude (*e.g.*, the conductivity of GM). In order to evaluate the effect of more educated priors on the computed metrics, we also defined a second input parameter space, Ω_{norm}, where we used the truncated normal distributions for each tissue. We drew 20 new conductivity profiles from this new space using the same technique (See Table S2b in supplementary material).

2.5 Regions of interest

As explained in Table 1, each electrode montage targets a specific ROI in the left hemisphere. To extract individual binary masks of these brain areas for each subject, we relied on three different cortical atlases: Brodmann [13], CP-MMP 1.0 [15] and MarsAtlas [4].

Unfortunately, the latter is not available in fsaverage space (*i.e.*, the standard space for *FreeSurfer* defined as a reference cortical surface) [34]. However, it has been published in Colin27 space [21]. To produce the proper labels in fsaverage space from MarsAtlas, we first converted the segmented volume into labels in the native space of the subject. Next, we registered these labels onto fsaverage cortical surface with the surface registration tools from *FreeSurfer* [9]. The resulting labels for the four ROIs are displayed on fsaverage in Figure 3.

Once all the labels were extracted and projected on fsaverage, we registered them on the cortical surfaces of each subject and converted them into binary masks coregistered on the SEG-05 images.

We also extracted the surface area (mm^2), the volume (mm^3) and the depth (mm) of these regions for all the subjects (See Table S3).

2.6 Simulations

We simulated tDCS with *Shamo* [17] which interfaces with *GetDP* [14] to solve the finite element problems. Each simulation solves the Poisson equation [10, 18]

$$\boldsymbol{\nabla} \cdot (\kappa \boldsymbol{\nabla}(v)) = -\rho_{\mathrm{s}}, \tag{1}$$

where v (V) is the electric potential and ρ_{s} (A m^{-3}) is the source volume current density. The boundary conditions were set so that the anode injected 2 mA and the cathode acted as a reference (i.e. 0 V).

Considering the 20 subjects, their respective 30 finite element models described in Section 2.2 with the electrode montages from Section 2.3 and the 21 different conductivity profiles drawn from $\Omega_{\mathrm{uniform}}$ defined in Section 2.4,

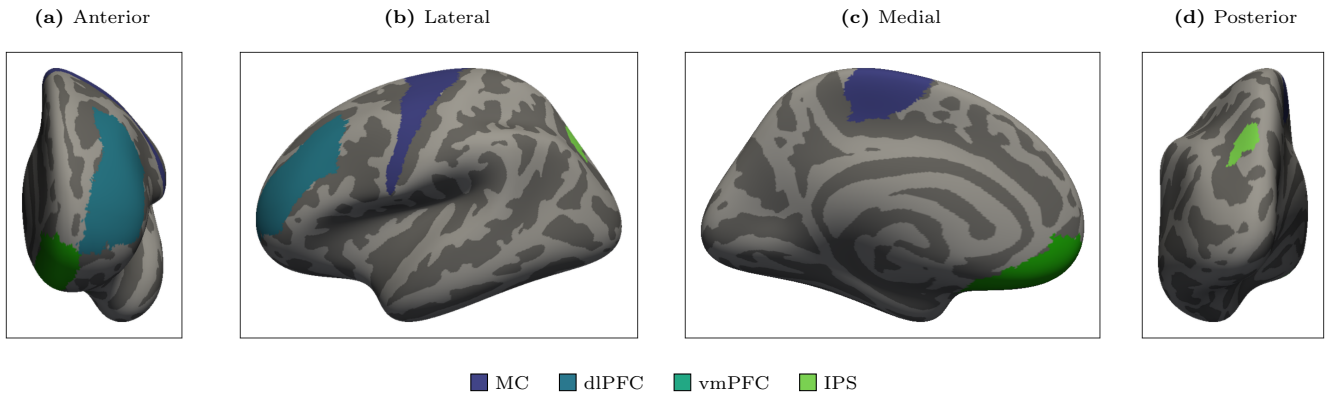

Fig. 3 The left hemisphere ROIs considered in this study and extracted from Brodmann [13], HCP-MMP 1.0 [15] and MarsAtlas [4] atlases displayed on the inflated surface of fsaverage.

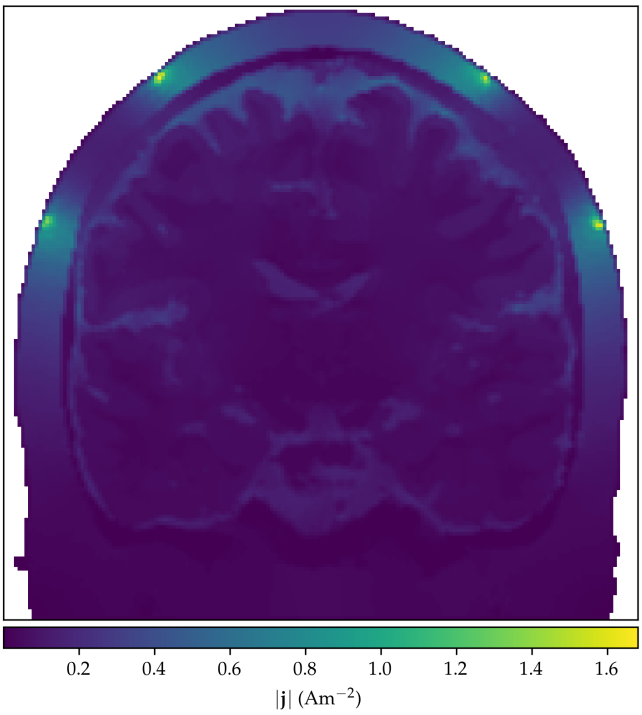

Fig. 4 A cut of the magnitude of the magnitude of the current density computed in the head of subject 4 resulting from the injection of 2 mA with the C3-C4 electrode montage.

we ran a total of 12600 simulations (2100 for each experiment).

The simulations calculated the electric potential v (V), the electric field $\boldsymbol{e}$ (V m^{-1}) and the current density $\boldsymbol{j}$ (A m^{-2}) on the unstructured meshes (See Figure 4). To make any further processing easier, we converted these fields into NIfTI files by sampling them on a regular $1\times1\times1$ mm^3 grid with the same orientation as the SEG-05 image.

Then, by applying the binary masks built in Section 2.5, we extracted the values of these fields for all the voxels of the ROIs in each simulation and stored it in a *DuckDB* database [41]. In addition, we computed both the components normal and tangential to the cortical surface of $\boldsymbol{e}$ and $\boldsymbol{j}$.

Finally, we computed the average absolute values for all the previously described metrics for each simulation.

2.7 Gaussian process regressors

As described above, we only performed simulations for the conductivity profiles drawn from Ω_{uniform}, while in Section 2.4 we stated that we also defined 20 conductivity profiles from Ω_{norm}.

Indeed, running the simulations is computationally expensive. In order to reduce the computation time required, and considering that the points drawn from Ω_{norm} are also included in Ω_{uniform}, we decided to fit multi-output Gaussian process regressors (GPR) [44] on the results of the simulations described in Section 2.6 using *scikit-learn* [38]. Following the recommendations from Chen et al. [8], the regression part of the GPR was set to the mean of the output variable and the kernel was defined as the product of a constant kernel and a stationary Matérn kernel with a smoothness parameter $\nu = 2.5$.

This way, we leveraged the 12600 simulations to interpolate the results corresponding to the conductivity profiles from Ω_{norm}.

2.8 Models

We focused on the mean absolute magnitude of the electric field $|\bar{\boldsymbol{e}}|$ and of its component normal to the cortical surface $|\bar{\boldsymbol{e}}_r|$. For each experiment, we built different Bayesian models using *Bambi* [7] which is based on *PyMC3* [49]. The basic expression of all these models is

$$Y \sim \mathcal{N}(\mu, \sigma^2), \tag{2}$$

with Y the dependent variable, μ defined as

$$\mu = \alpha + \boldsymbol{\beta} \cdot \boldsymbol{X} + \varepsilon, \tag{3}$$

where α the intercept, $\boldsymbol{\beta} = [\beta_1, \ldots, \beta_n]$ the slopes, $\boldsymbol{X} = [X_1, \ldots, X_n]^\top$ the vector of independent variables and ε the error term. We also consider the hierarchic counterpart of these pooled models, in which we account for the subject with a random effect. For these models, we have different values of μ, α and $\boldsymbol{\beta}$ for each subject i,

$$\begin{aligned} \mu_i &= \alpha_i + \boldsymbol{\beta_i} \cdot \boldsymbol{X} + \varepsilon, \\ \alpha_i &= \alpha^{(\text{com})} + \alpha_i^{(\text{sub})}, \\ (\beta_j)_i &= \beta_j^{(\text{com})} + (\beta_j^{(\text{sub})})_i, \end{aligned} \tag{4}$$

where $\alpha^{(\text{com})}$ and $\beta_j^{(\text{com})}$ are respectively the common intercept and slopes and $\alpha_i^{(\text{sub})}$ and $(\beta_j^{(\text{sub})})_i$ are the subject specific contributions to the intercept and slopes.

For all the models described in the next paragraphs, weakly informative priors are set automatically using the method explained in Westfall [58]. They are then all fitted using the No-U-Turn sampler (NUTS) [20] with 4 chains of 1000 tune and 1000 draw iterations.

To decide whether a parameter has a significant effect on the dependent variable, we use the 95 % highest density interval (HDI) and the "region of practical evidence" (ROPE) around the null value [29]. This method states that if the 95 % HDI lies inside the ROPE for more than 97.5 %, the corresponding parameter is null (the 95 % most credible values of the parameter are all practically equivalent to the null value). Conversely, if the 95 % HDI intersects with the ROPE for less than 2.5 %, the parameter is non-null. Finally, if the intersection between the two intervals is between these two boundaries, we cannot conclude whether the parameter is null or not. The boundaries of the ROPE are set to $\pm 0.1 \cdot \text{std}(Y)$.

2.8.1 Anode placement

To evaluate the effect of a displacement of 1 cm of the anode with regard to the reference EEG 10-20 position, we define a model to assess the difference between the measurements computed for each of the 5 anode placements from Section 2.3 as

$$\begin{aligned} \mu &= \alpha + \sum_{p=1}^{4} \beta_p \cdot X_p + \varepsilon, \\ \mu_i &= \alpha_i + \sum_{p=1}^{4} (\beta_p)_i \cdot X_p + \varepsilon, \end{aligned} \tag{5}$$

where p corresponds to a specific displacement of the anode (anterior, central, lateral or posterior) and X_p is either 0 or 1 based on the anode used to obtain the record.

2.8.2 Conductivity profile

Using the same method, we compare the values of both $|\bar{e}|$ and $|\bar{e}_r|$ calculated for the 20 conductivity profiles described in Section 2.4 with the values obtained for the reference profile, where the conductivity of each tissue is set to the value recommended by McCann et al. [33]. Thus, we transform the base models from Equation 3 and 4 into

$$\begin{aligned} \mu &= \alpha + \sum_{k=1}^{20} \beta_k \cdot X_k + \varepsilon, \\ \mu_i &= \alpha_i + \sum_{k=1}^{20} (\beta_k)_i \cdot X_k + \varepsilon. \end{aligned} \tag{6}$$

In these expressions, k refers to one of the 20 conductivity profiles established using the quasi-random Halton sequence and X_k is 1 or 0.

2.8.3 Bipolar and unipolar electrode montages

As shown in Table 1, we simulate a bipolar and an unipolar electrode montage to stimulate both the MC and the dlPFC. In order to compare the values of $|\bar{e}|$ and $|\bar{e}_r|$ computed for each pairs, we fit the models with the following expected values,

$$\begin{aligned} \mu &= \alpha + \beta_{\text{uni}} \cdot X_{\text{uni}} + \varepsilon, \\ \mu_i &= \alpha_i + (\beta_{\text{uni}})_i \cdot X_{\text{uni}} + \varepsilon, \end{aligned} \tag{7}$$

with X_{uni} equal either to 1 if the montage is unipolar or to 0 otherwise.

2.9 Induced trans-membrane potential

The steady-state induced trans-membrane potential (ITP), denoted by Δu_{i} (mV), is the potential difference measured between the inside u_{in} and the outside u_{out} of the cell membrane added to the resting state potential Δu_{r} and due to an external stimulation,

$$u_{\text{in}} - u_{\text{out}} = \Delta u_{\text{r}} + \Delta u_{\text{i}}. \tag{8}$$

While tDCS is not able to trigger action potentials, it is generally accepted that it generates an induced trans-membrane potential which hyperpolarizes the neuron membranes under the anode and depolarizes it under the cathode [39, 55]. In the present work, we compute the ITP resulting from the different stimulations using analytical expressions for both spherical and spheroidal cells.

2.9.1 Spherical cell

The theoretical steady-state ITP resulting from an external electric field $\boldsymbol{e}$ (V m^{-1}) in a spherical cell of radius r_1 (m) with a non-conductive plasma membrane is described by Schwan's equation [51]

$$\Delta u_{\text{i}} = \frac{3}{2} |\boldsymbol{e}| r_1 \cos(\theta), \tag{9}$$

with θ the angle between the electric field and the vector going from the centre of the cell to the point of the membrane where the ITP is calculated.

Consequently, the maximum value of Δu_{i} is obtained for $\theta = 0$. To avoid using an arbitrary value for r_1, we finally compute

$$\frac{\max(\Delta u_{\text{i}})}{r_1} = \frac{3}{2} |\boldsymbol{e}|. \tag{10}$$

2.9.2 Spheroidal cell

Pyramidal cortical cells are not spherical, thus we also consider spheroidal cells $r_1 > r_2 = r_3$ with a shape ratio $\gamma = r_1/r_2$ and elongated along the normal of the cortical surface. For such cells, Valic et al. [56] gives the following expression of the ITP,

$$\Delta u_{\text{i}} = |\boldsymbol{e}| \sin(\varphi) \frac{r_2 \sin(\theta)}{1 - l_x} + |\boldsymbol{e}| \cos(\varphi) \frac{r_1 \cos(\theta)}{1 - l_z}, \tag{11}$$

where φ is the angle between the electric field and the main axis of the cell and l_x and l_z are the depolarization factors

$$l_z = \frac{1 - \lambda^2}{2\lambda^3} \left(\log\left(\frac{1 + \lambda}{1 - \lambda} \right) - 2\lambda \right), \tag{12}$$

$$l_x = \frac{1}{2}(1 - l_z), \tag{13}$$

with $\lambda = \sqrt{1 - (1/\gamma)^2}$.

Since we already computed the tangential and radial components of the electric field denoted by $|\boldsymbol{e}_t|$ and $|\boldsymbol{e}_r|$, we have

$$\Delta u_{\text{i}} = |\boldsymbol{e}_t| \frac{r_2 \sin(\theta)}{1 - l_x} + |\boldsymbol{e}_r| \frac{r_1 \cos(\theta)}{1 - l_z}, \tag{14}$$

which is maximized when

$$\theta = \theta_{\max} = \operatorname{atan}\left(\frac{|\boldsymbol{e}_t|(1-l_z)}{|\boldsymbol{e}_r|\gamma(1-l_z)}\right). \tag{15}$$

Following what we did for the spherical cell, we derive the size independent expression

$$\frac{\max(\Delta u_{\mathrm{i}})}{r_1} = |\boldsymbol{e}_t|\frac{\sin(\theta_{\max})}{\gamma(1-l_x)} + |\boldsymbol{e}_r|\frac{\cos(\theta_{\max})}{1-l_z}. \tag{16}$$

3 Results

Figure 5 shows the distributions of the measured values of $|\bar{\boldsymbol{e}}|$ and $|\bar{\boldsymbol{e}_r}|$ ($\mathrm{mV\,m^{-1}}$) for the different experiments defined in Table 1 (See also Figures S21-32a-b). Overall, the mean absolute magnitude of the electric field ranges from 47.2 to 644.2 $\mathrm{mV\,m^{-1}}$ and its component normal to the cortical surface from 24.2 to 470.7 $\mathrm{mV\,m^{-1}}$ for the simulations, while for the GPRs, $|\bar{\boldsymbol{e}}|$ ranges from 139.2 to 398.5 $\mathrm{mV\,m^{-1}}$ and $|\bar{\boldsymbol{e}_r}|$ ranges from 69.5 to 223.9 $\mathrm{mV\,m^{-1}}$.

In order to better picture the results, we show the data obtained for the C3-C4 electrode montage targeting the motor cortex, based on the conductivity profiles drawn from $\Omega_{\mathrm{uniform}}$, all along the following sections. Figure 6 shows the results for this specific montage, and the outcome of the other experiments are provided in supplementary materials.

3.1 Anode placement

Based on the measurements acquired for each anode placements shown in Figure 7 for the C3-C4 electrode montage (See Figures S22-32e-f for the other experiments), we fitted the model from Equation 5 and computed the 95 % HDI of β_p and $\beta_p^{(\mathrm{com})}$ which are given in Tables S4/8a-b.

Overall, for the results obtained using $\Omega_{\mathrm{uniform}}$, most of the 95 % HDI intercept with the ROPE for more than 2.5 % but none of them is fully included (*i.e.*, more than 97.5 %) in the ROPE. Consequently, we cannot state whether an error of 1 cm on the placement of the anode plays a significant role or not in the electric field induced in the ROIs.

However, by computing the boundaries of the absolute ratio between the values of β_p and the intercept, we get that such an error on the anode placement yields an absolute relative difference with the reference value up to 27.6 % for $|\bar{\boldsymbol{e}}|$ and up to 27.1 % % for $|\bar{\boldsymbol{e}_r}|$.

When moving to Ω_{norm}, the trend is reversed and most of the 95 % HDI do not intercept with the ROPE, while the maximum absolute ratios between the values of β_p and the intercept drop to 18.5 % and 17.6 % for $|\bar{\boldsymbol{e}}|$ and $|\bar{\boldsymbol{e}_r}|$ respectively.

3.2 Tissues electrical conductivity

Similarly to the anode placement, Figure 8 shows the results for the C3-C4 montage (See Figures S22-32c-d for the other experiments).

Following the descriptions of the pooled and hierarchic models from Equation 6, we determined values for each β_k and $\beta_k^{(\mathrm{com})}$ for both $|\bar{\boldsymbol{e}}|$ and $|\bar{\boldsymbol{e}_r}|$ (See Tables S7/11a-b for the 95 % HDI).

As opposed to the anode placement, the majority of the 95 % HDI computed on $\Omega_{\mathrm{uniform}}$ fall completely outside the ROPE, meaning that the uncertainty on the conductivity of the tissues has a significant influence on the electric field computed in the ROI.

Moreover, by calculating the same absolute ratio between the different β_k and α, we found that some conductivity profiles could induce a difference relative to the reference of up to 112.5 % and 146.6 % for $|\bar{\boldsymbol{e}}|$ and $|\bar{\boldsymbol{e}_r}|$ respectively.

Once again, using Ω_{norm} inverses the trend and all the computed 95 % HDI intercept for more than 2.5 % with the ROPE, and some are fully embedded in, meaning that changing the conductivity profile yields easier no significant variation or a variation that cannot be classified as significant or not. The maximum ratios obtained for these results drop considerably when compared to those obtained from $\Omega_{\mathrm{uniform}}$. Indeed, the values are 13.1 % for $|\bar{\boldsymbol{e}}|$ and 14.2 % for $|\bar{\boldsymbol{e}_r}|$.

3.3 Bipolar and unipolar electrode montages

Figure 9 provides an overview of the metrics of interest computed for the two electrode montages targeting the motor cortex.

By fitting the model from Equation 7, we determined the difference between the results computed for the bipolar and unipolar electrode montages targeting both the motor cortex and the dorsolateral prefrontal cortex (See Table S5/9a-b for the 95 % HDI of $\beta_{\mathrm{uni}}^{(\mathrm{com})}$).

Using the unipolar montage when stimulating the MC yields an electric field of up to 13.7 % lower than with the bipolar montage for both $\Omega_{\mathrm{uniform}}$ and Ω_{norm}. However, the effect on the normal component of the electric field is not determined when considering $\Omega_{\mathrm{uniform}}$ but is significant for Ω_{norm}.

On the other hand, both montages yield equivalent normal components of the electric field when targeting the dlPFC.

3.4 Induced transmembrane potential

As described in Section 2.9, we computed the induced transmembrane potential resulting from the electric field generated in the ROIs for the different electrode montages using analytical expressions for spherical and spheroidal cells. The calculated ranges of $\Delta u_{\mathrm{i}}/r_1$ are shown in Table S6/10.

Across all the experiments, the spherical and spheroidal cell models respectively yield values ranging from 70.9 to 966.3 $\mathrm{mV\,m^{-1}}$ and from 21.5 to 441.5 $\mathrm{mV\,m^{-1}}$ when considering $\Omega_{\mathrm{uniform}}$ and from 208.9 to 597.7 $\mathrm{mV\,m^{-1}}$ and 62.3 to 209.8 $\mathrm{mV\,m^{-1}}$ when using Ω_{norm}.

4 Discussion

The results of the models assessing the effect of different conductivity profiles in $\Omega_{\mathrm{uniform}}$ are concerning. As for the anode placement, the F3-Fp2 electrode montage is the most influenced, with a difference of up to 112.5 % on $|\bar{\boldsymbol{e}}|$. Still, it is interesting to note that the direction of the

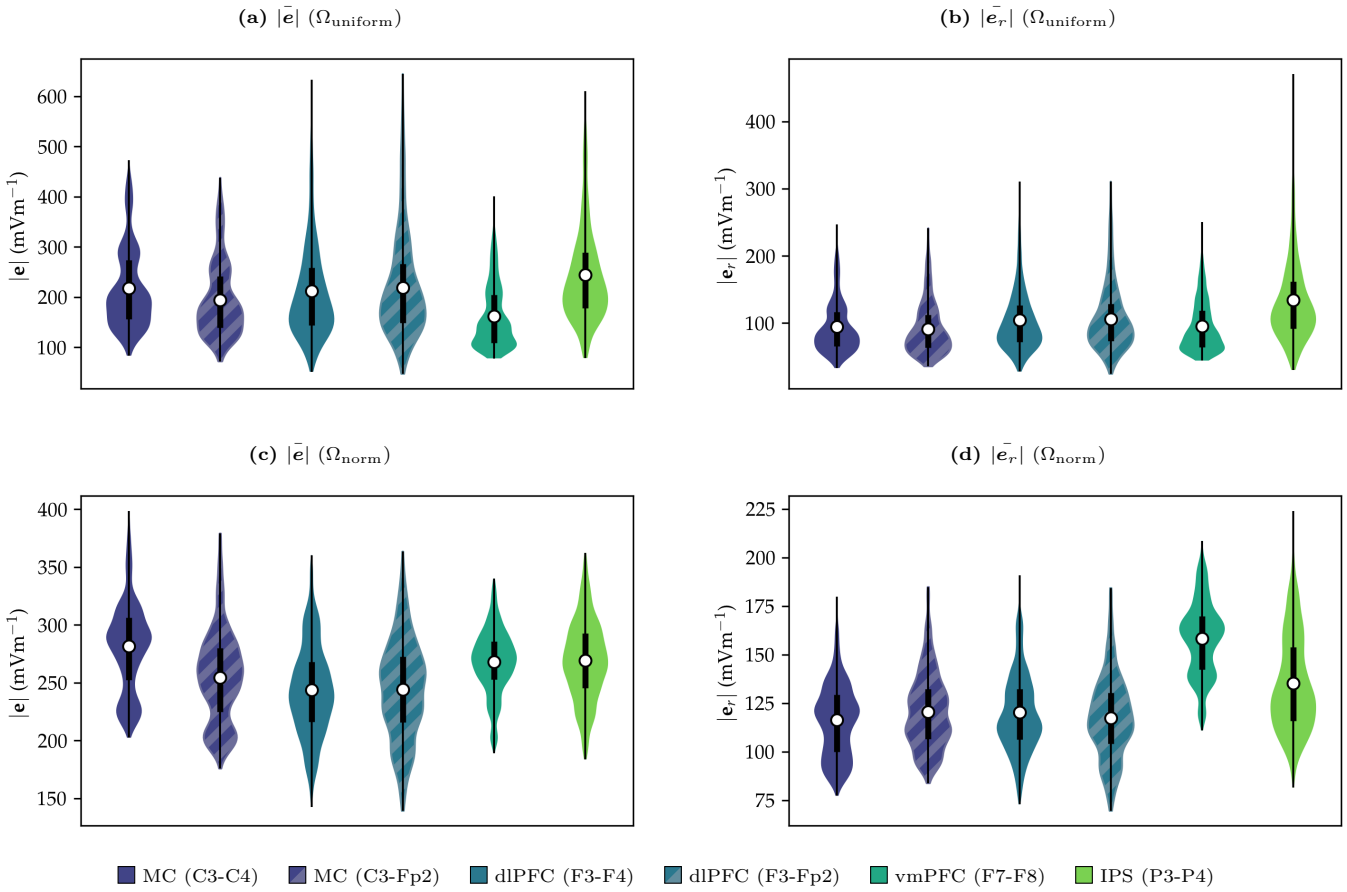

Fig. 5 (a/c) The average absolute magnitude of the electric field $|\bar{e}|$ and **(b/d)** the average absolute magnitude of the normal component of the electric field $|\bar{e_r}|$ recorded for all the simulations for the different ROIs and electrode montages.

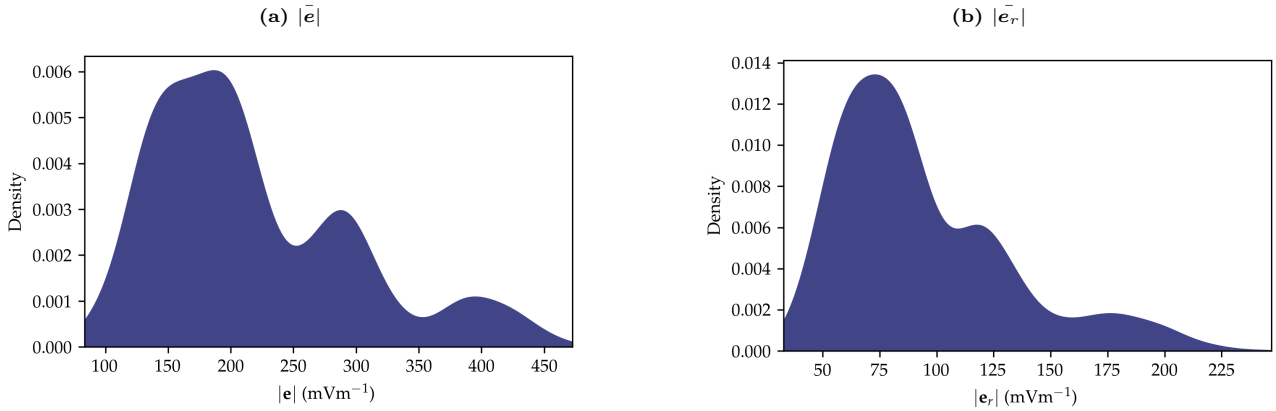

Fig. 6 The average absolute value of **(a)**the magnitude of the electric field and **(b)** its radial component for the C3-C4 electrode montage targeting the motor cortex.

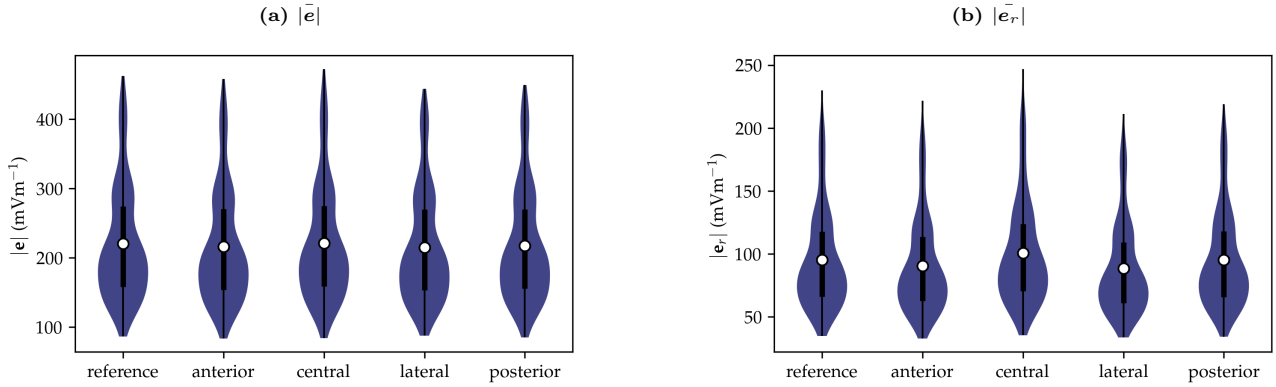

Fig. 7 The average absolute value of **(a)**the magnitude of the electric field and **(b)** its radial component for the C3-C4 electrode montage targeting the motor cortex, grouped by anode placements.

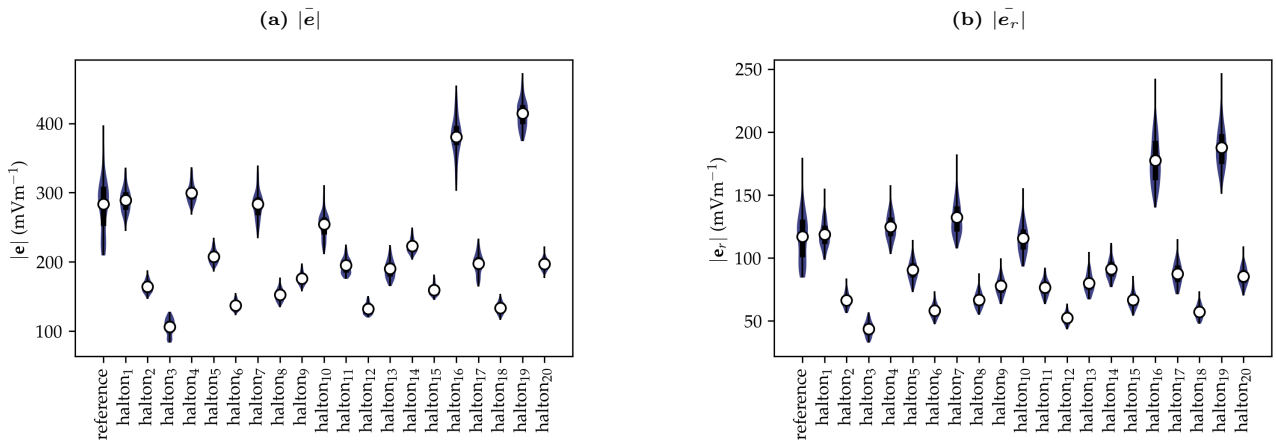

Fig. 8 The average absolute value of **(a)**the magnitude of the electric field and **(b)** its radial component for the C3-C4 electrode montage targeting the motor cortex, grouped by conductivity profiles.

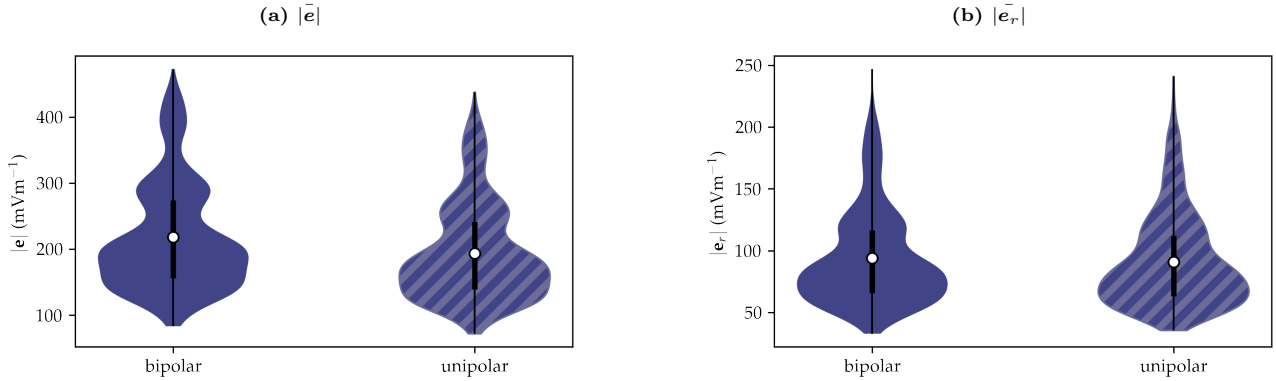

Fig. 9 The average absolute value of **(a)**the magnitude of the electric field and **(b)** its radial component for the uni- and bi-lateral electrode montages targeting the motor cortex.

electric field varies the most in the IPS when using the P3-P4 electrode montage. Indeed, the maximum relative difference can be up to 146.6 % on $|\bar{e_r}|$.

Still, for all the experiments, moving from the worst case scenario, where Ω_{uniform} is considered, to more educated priors on the conductivity of the tissues, when Ω_{norm} is used, yields a considerable drop in the variability of the computed metrics, which end up lower than 15 %. This also affects the other Bayesian linear models. Indeed, when the uncertainty lying in the conductivity is reduced, the influence of the other factors grow.

On the other hand, the results we obtained regarding the error on the anode placement are in line with the ones published by Ramaraju et al. [43]. Indeed, we find that the F3-Fp2 electrode montage is more sensitive to the anode placement than the others. However, the 27.6 % change in the mean absolute electric field in the left dlPFC is comparable with the 38 % they measured in the left frontal lobe. When improving the priors on the conductivity of the tissues, the error on the anode placement becomes significant in most of the cases, but the maximum error decreases to around 18 %.

While such a difference is non-negligible, it results from a displacement of 1 cm of the anode. Considering the work of Rich and Gillick [46] which showed that the inter- and intra-rater error on the electrode placement is lower than 1 cm, the shift in the anode position we studied can be regarded as an upper bound to the plausible experimental deviation. As a result, the actual variation of the electric field induced in the ROI due to a misplaced electrode is expected to be smaller than what we calculated here.

These considerable variations obtained with Ω_{uniform} lead us to question the information we can extract from modelling tDCS. Until one cannot feed the models with better priors about the electrical conductivity of the biological tissues, the randomness of the outputs makes it almost impossible to gain insights and draw conclusions about the electric effect of the stimulation. Using Ω_{norm} resulted in a significant improvement of the outcome, but, even though the electric conductivities of a random subject are more likely to remain closer to the reported mean, nothing prevents them to drift toward the extrema.

Moreover, the conventional way of modelling tDCS, which involves setting almost arbitrary values to the electrical conductivity of the tissues based on the literature, identical for each subject, appears to be an inappropriate assumption.

Techniques such as magnetic resonance electric impedance tomography (MREIT) [61] and conductivity tensor imaging (CTI) [32] could provide a better description of the electric properties of the tissues of each subject.

Finally, tDCS is expected to generate an induced transmembrane potential of around 0.5 mV in the neurons of the target ROI [37, 42]. The values we obtain analytically, considering $r_1 = 1$ mm, are at most of the same order of magnitude but can be smaller by up to a factor of 20.

Once again, this value relies heavily on the conductiv-

ity profile of the models. Still, computing ITP values of 0.02 mV, as compared to a resting potential of −70 mV and a reference action potential threshold of −55 mV, highlights the questionable efficiency of tDCS as a neuromodulation technique. This concern has already been raised by other papers before [22].

Still, it is important to mention that, since the present study only focused on simulations, we cannot draw conclusions on the functional long-lasting effect of the different experiments.

5 Conclusion

In the present work, we studied the influence of an error of placement of the anode and of the unknown conductivity profile on the computed electric field resulting from 6 different tDCS experiment targeting 4 ROIs on 20 subjects using a simulation tool. A total of 12600 simulations were performed.

The models used in this paper show that anode displacements of reasonable size yield a negligible to moderate effect on the electric field induced in the ROI. They also highlight that the uncertainty regarding the electrical conductivity of the tissues make it practically impossible to assess the electrical effect of the stimulation in a specific ROI and that using fixed standard values could potentially yield highly biased results. The comparison between Ω_{uniform} and Ω_{norm} clearly shows that using more informative priors reduces the variability of the output.

Improving the conductivity acquisition methods could lead to a better understanding of the factors that underly the variability of the effects of tDCS experiments. Until no new method is proposed to measure tissues electric conductivity on a subject basis, using uncertainty quantification and sensitivity analysis with *Shamo* or other similar tools could allow for more educated conclusions.

We also computed the induced transmembrane potential induced by the stimulation for different simple cell models. The overall size of the computed ITP is concerning.

While we did not perform functional experiments in parallel to the modelling work, the overall results presented here lead us to call for caution when designing, modelling and analysing a tDCS experiment.

Data sharing

The results from the different preprocessing steps are reported in the supplementary materials section, and the notebooks used to compute the results presented in this paper are available at [**TODO:** Link to repository].

The code for Shamo is available on Github[3].

Acknowledgements

The study have been supported by the Fonds de la Recherche Scientifique de Belgique (F.R.S.-F.N.R.S.) under Grant No. EOS 30446199.

Computational resources have been provided by the Consortium des Équipements de Calcul Intensif (CÉCI), funded by the Fonds de la Recherche Scientifique de Belgique (F.R.S.-FNRS) under Grant No. 2.5020.11 and by the Walloon Region.

References

[1] Alejandro Albizu, Ruogu Fang, Aprinda Indahlastari, Andrew O'Shea, Skylar E. Stolte, Kyle B. See, Emanuel M. Boutzoukas, Jessica N. Kraft, Nicole R. Nissim, and Adam J. Woods. Machine learning and individual variability in electric field characteristics predict tDCS treatment response. *Brain Stimulation*, 13(6):1753–1764, November 2020. ISSN 1935-861X. doi: 10.1016/j.brs.2020.10.001. URL https://www.sciencedirect.com/science/article/pii/S1935861X20302680.

[2] Berengere Aubert-Broche, Alan C. Evans, and Louis Collins. A new improved version of the realistic digital brain phantom. *NeuroImage*, 32(1):138–145, August 2006. ISSN 1053-8119. doi: 10.1016/j.neuroimage.2006.03.052.

[3] Berengère Aubert-Broche, Mark Griffin, G. Bruce Pike, Alan C. Evans, and D. Louis Collins. Twenty new digital brain phantoms for creation of validation image data bases. *IEEE transactions on medical imaging*, 25(11):1410–1416, November 2006. ISSN 0278-0062. doi: 10.1109/TMI.2006.883453.

[4] Guillaume Auzias, Olivier Coulon, and Andrea Brovelli. MarsAtlas: A cortical parcellation atlas for functional mapping. *Human Brain Mapping*, 37(4):1573–1592, 2016. ISSN 1097-0193. doi: 10.1002/hbm.23121. URL https://onlinelibrary.wiley.com/doi/abs/10.1002/hbm.23121. _eprint: https://onlinelibrary.wiley.com/doi/pdf/10.1002/hbm.23121.

[5] Paulo S. Boggio, Alice Nunes, Sergio P. Rigonatti, Michael A. Nitsche, Alvaro Pascual-Leone, and Felipe Fregni. Repeated sessions of noninvasive brain DC stimulation is associated with motor function improvement in stroke patients. *Restorative Neurology and Neuroscience*, 25(2):123–129, 2007. ISSN 0922-6028.

[6] Matthew Brett, Christopher J. Markiewicz, Michael Hanke, Marc-Alexandre Côté, Ben Cipollini, Paul McCarthy, Dorota Jarecka, Christopher P. Cheng, Yaroslav O. Halchenko, Michiel Cottaar, and et al. nipy/nibabel: 3.2.1. Nov 2020. doi: 10.5281/zenodo.4295521.

[7] Tomás Capretto, Camen Piho, Ravin Kumar, Jacob Westfall, Tal Yarkoni, and Osvaldo A. Martin. Bambi: A simple interface for fitting bayesian linear models in python, 2020.

[8] Hao Chen, Jason L. Loeppky, Jerome Sacks, and William J. Welch. Analysis Methods for Computer Experiments: How to Assess and What Counts? *Statistical Science*, 31(1):40–60, February 2016. ISSN 0883-4237. doi: 10.1214/15-STS531. URL http://projecteuclid.org/euclid.ss/1455115913.

[9] Anders M. Dale, Bruce Fischl, and Martin I. Sereno. Cortical Surface-Based Analysis: I. Segmentation and Surface Reconstruction. *NeuroImage*, 9(2):179–194, February 1999. ISSN 1053-8119. doi: 10.1006/nimg.1998.0395. URL https://www.sciencedirect.com/science/article/pii/S1053811998903950.

[10] Marion Darbas and Stephanie Lohrengel. Review on Mathematical Modelling of Electroencephalography (EEG). *Jahresbericht der Deutschen Mathematiker-Vereinigung*, July 2018. doi: 10.1365/s13291-018-0183-z.

[11] Josefien Dedoncker, Andre R. Brunoni, Chris Baeken, and Marie-Anne Vanderhasselt. A Systematic Review and Meta-Analysis of the Effects of Transcranial Direct Current Stimulation (tDCS) Over the Dorsolateral Prefrontal Cortex in Healthy and Neuropsychiatric Samples: Influence of Stimulation Parameters. *Brain Stimulation: Basic, Translational, and Clinical Research in Neuromodulation*, 9(4):501–517, July 2016. ISSN 1935-861X, 1876-4754. doi: 10.1016/j.brs.2016.04.006. URL https://www.brainstimjrnl.com/article/S1935-861X(16)30056-0/fulltext. Publisher: Elsevier.

3. https://github.com/CyclotronResearchCentre/shamo

[12] Romain Dumont, Steve Majerus, and Michel Hansenne. Transcranial Direct Current Stimulation (tDCS) over the Intraparietal Sulcus Does Not Influence Working Memory Performance. *Psychologica Belgica*, 61(1):200–211, July 2021. ISSN 2054-670X. doi: 10.5334/pb.534. URL http://www.psychologicabelgica.com/articles/10.5334/pb.534/. Number: 1 Publisher: Ubiquity Press.

[13] Bruce Fischl, Niranjini Rajendran, Evelina Busa, Jean Augustinack, Oliver Hinds, B. T. Thomas Yeo, Hartmut Mohlberg, Katrin Amunts, and Karl Zilles. Cortical folding patterns and predicting cytoarchitecture. *Cerebral Cortex (New York, N.Y.: 1991)*, 18(8):1973–1980, August 2008. ISSN 1460-2199. doi: 10.1093/cercor/bhm225.

[14] C. Geuzaine. GetDP: a general finite-element solver for the de Rham complex. In *PAMM Volume 7 Issue 1. Special Issue: Sixth International Congress on Industrial Applied Mathematics (ICIAM07) and GAMM Annual Meeting, Zürich 2007*, volume 7, pages 1010603–1010604. Wiley, 2008.

[15] Matthew F. Glasser, Timothy S. Coalson, Emma C. Robinson, Carl D. Hacker, John Harwell, Essa Yacoub, Kamil Ugurbil, Jesper Andersson, Christian F. Beckmann, Mark Jenkinson, Stephen M. Smith, and David C. Van Essen. A multi-modal parcellation of human cerebral cortex. *Nature*, 536(7615):171–178, August 2016. ISSN 1476-4687. doi: 10.1038/nature18933. URL https://www.nature.com/articles/nature18933.

[16] Krzysztof J. Gorgolewski, Tibor Auer, Vince D. Calhoun, R. Cameron Craddock, Samir Das, Eugene P. Duff, Guillaume Flandin, Satrajit S. Ghosh, Tristan Glatard, Yaroslav O. Halchenko, Daniel A. Handwerker, Michael Hanke, David Keator, Xiangrui Li, Zachary Michael, Camille Maumet, B. Nolan Nichols, Thomas E. Nichols, John Pellman, Jean-Baptiste Poline, Ariel Rokem, Gunnar Schaefer, Vanessa Sochat, William Triplett, Jessica A. Turner, Gaël Varoquaux, and Russell A. Poldrack. The brain imaging data structure, a format for organizing and describing outputs of neuroimaging experiments. *Scientific Data*, 3(1):160044, June 2016. ISSN 2052-4463. doi: 10.1038/sdata.2016.44. URL https://www.nature.com/articles/sdata201644.

[17] Martin Grignard, Christophe Geuzaine, and Christophe Phillips. Shamo: A Tool for Electromagnetic Modeling, Simulation and Sensitivity Analysis of the Head. *Neuroinformatics*, March 2022. ISSN 1559-0089. doi: 10.1007/s12021-022-09574-7. URL https://doi.org/10.1007/s12021-022-09574-7.

[18] Hans Hallez, Bart Vanrumste, Roberta Grech, Joseph Muscat, Wim De Clercq, Anneleen Vergult, Yves D'Asseler, Kenneth P. Camilleri, Simon G. Fabri, Sabine Van Huffel, and Ignace Lemahieu. Review on solving the forward problem in EEG source analysis. *Journal of NeuroEngineering and Rehabilitation*, 4(1):46, November 2007. ISSN 1743-0003. doi: 10.1186/1743-0003-4-46. URL https://doi.org/10.1186/1743-0003-4-46.

[19] J. H. Halton. On the efficiency of certain quasi-random sequences of points in evaluating multi-dimensional integrals. *Numerische Mathematik*, 2(1):84–90, December 1960. ISSN 0029-599X, 0945-3245. doi: 10.1007/BF01386213. URL http://link.springer.com/10.1007/BF01386213.

[20] Matthew D. Hoffman and Andrew Gelman. The No-U-Turn Sampler: Adaptively Setting Path Lengths in Hamiltonian Monte Carlo. *arXiv:1111.4246 [cs, stat]*, November 2011. URL http://arxiv.org/abs/1111.4246. arXiv: 1111.4246.

[21] Colin J. Holmes, Rick Hoge, Louis Collins, Roger Woods, Arthur W. Toga, and Alan C. Evans. Enhancement of MR Images Using Registration for Signal Averaging. *Journal of Computer Assisted Tomography*, 22(2):324–333, April 1998. ISSN 0363-8715. URL https://journals.lww.com/jcat/Abstract/1998/03000/Enhancement_of_MR_Images_Using_Registration_for.32.aspx.

[22] Jared Cooney Horvath, Jason D. Forte, and Olivia Carter. Evidence that transcranial direct current stimulation (tDCS) generates little-to-no reliable neurophysiologic effect beyond MEP amplitude modulation in healthy human subjects: A systematic review. *Neuropsychologia*, 66:213–236, January 2015. ISSN 00283932. doi: 10.1016/j.neuropsychologia.2014.11.021. URL https://linkinghub.elsevier.com/retrieve/pii/S0028393214004394.

[23] Liron Jacobson, Meni Koslowsky, and Michal Lavidor. tDCS polarity effects in motor and cognitive domains: a meta-analytical review. *Experimental Brain Research*, 216(1):1–10, January 2012. ISSN 0014-4819, 1432-1106. doi: 10.1007/s00221-011-2891-9. URL http://link.springer.com/10.1007/s00221-011-2891-9.

[24] Noa Jacoby and Michal Lavidor. Null tDCS Effects in a Sustained Attention Task: The Modulating Role of Learning. *Frontiers in Psychology*, 9:476, April 2018. ISSN 1664-1078. doi: 10.3389/fpsyg.2018.00476. URL http://journal.frontiersin.org/article/10.3389/fpsyg.2018.00476/full.

[25] H Jasper. Report of the committee on methods of clinical examination in electroencephalography: 1957. *Electroencephalography and Clinical Neurophysiology*, 10(2):370–375, May 1958. ISSN 0013-4694. doi: 10.1016/0013-4694(58)90053-1. URL https://www.sciencedirect.com/science/article/pii/0013469458900531.

[26] Valer Jurcak, Masako Okamoto, Archana Singh, and Ippeita Dan. Virtual 10-20 measurement on MR images for inter-modal linking of transcranial and tomographic neuroimaging methods. *NeuroImage*, 26(4):1184–1192, July 2005. ISSN 1053-8119. doi: 10.1016/j.neuroimage.2005.03.021.

[27] G. H. Klem, H. O. Lüders, H. H. Jasper, and C. Elger. The ten-twenty electrode system of the International Federation. The International Federation of Clinical Neurophysiology. *Electroencephalography and Clinical Neurophysiology. Supplement*, 52:3–6, 1999. ISSN 0424-8155.

[28] Juri D. Kropotov. Chapter 4.4 - Transcranial Direct Current Stimulation. In Juri D. Kropotov, editor, *Functional Neuromarkers for Psychiatry*, pages 273–280. Academic Press, San Diego, January 2016. ISBN 978-0-12-410513-3. doi: 10.1016/B978-0-12-410513-3.00018-8.

[29] John K. Kruschke and Torrin M. Liddell. The Bayesian New Statistics: Hypothesis testing, estimation, meta-analysis, and power analysis from a Bayesian perspective. *Psychonomic Bulletin & Review*, 25(1):178–206, February 2018. ISSN 1531-5320. doi: 10.3758/s13423-016-1221-4.

[30] Caixia Li, Sukunya Jirachaipitak, Paul Wrigley, Hua Xu, and Pramote Euasobhon. Transcranial direct current stimulation for spinal cord injury-associated neuropathic pain. *The Korean Journal of Pain*, 34(2):156–164, April 2021. ISSN 2005-9159. doi: 10.3344/kjp.2021.34.2.156.

[31] Donna M. Lloyd, Priscilla G. Wittkopf, Laura J. Arendsen, and Anthony K. P. Jones. Is Transcranial Direct Current Stimulation (tDCS) Effective for the Treatment of Pain in Fibromyalgia? A Systematic Review and Meta-Analysis. *The Journal of Pain*, 21(11-12):1085–1100, December 2020. ISSN 1528-8447. doi: 10.1016/j.jpain.2020.01.003.

[32] Marco Marino, Lucilio Cordero-Grande, Dante Mantini, and Giulio Ferrazzi. Conductivity Tensor Imaging of the Human Brain Using Water Mapping Techniques. *Frontiers in Neuroscience*, 15, 2021. ISSN 1662-453X. URL https://www.frontiersin.org/article/10.3389/fnins.2021.694645.

[33] Hannah McCann, Giampaolo Pisano, and Leandro Beltrachini. Variation in Reported Human Head Tissue Electrical Conductivity Values. *Brain Topography*, 32(5):825–858, September 2019. ISSN 0896-0267, 1573-6792. doi: 10.1007/s10548-019-00710-2. URL http://link.springer.com/10.1007/s10548-019-00710-2.

[34] Kathryn Mills. Hcp-mmp1.0 projected on fsaverage, Jul 2016. URL https://figshare.com/articles/dataset/HCP-MMP1_0_projected_on_fsaverage/3498446/2.

[35] J. Florian M. Müller-Dahlhaus, Yuriy Orekhov, Yali Liu, and Ulf Ziemann. Interindividual variability and age-dependency of motor cortical plasticity induced by paired associative stimulation. *Experimental Brain Research*, 187(3):467–475, May 2008. ISSN 1432-1106. doi: 10.1007/s00221-008-1319-7. URL https://doi.org/10.1007/s00221-008-1319-7.

[36] Michael A. Nitsche, Leonardo G. Cohen, Eric M. Wassermann, Alberto Priori, Nicolas Lang, Andrea Antal, Walter Paulus, Friedhelm Hummel, Paulo S. Boggio, Felipe Fregni, and Alvaro Pascual-Leone. Transcranial direct current stimulation: State of the art 2008. *Brain Stimulation*, 1(3):206–223, July 2008. ISSN 1876-4754. doi: 10.1016/j.brs.2008.06.004.

[37] Alexander Opitz, Arnaud Falchier, Chao-Gan Yan, Erin M. Yeagle, Gary S. Linn, Pierre Megevand, Axel Thielscher, Ross Deborah A., Michael P. Milham, Ashesh D. Mehta, and Charles E. Schroeder. Spatiotemporal structure of intracranial electric fields induced by transcranial electric stimulation in humans and nonhuman primates. *Scientific Reports*, 6(1): 31236, August 2016. ISSN 2045-2322. doi: 10.1038/srep31236. URL https://www.nature.com/articles/srep31236. Number: 1 Publisher: Nature Publishing Group.

[38] Fabian Pedregosa, Gaël Varoquaux, Alexandre Gramfort, Vincent Michel, Bertrand Thirion, Olivier Grisel, Mathieu Blondel, Peter Prettenhofer, Ron Weiss, Vincent Dubourg, Jake Vanderplas, Alexandre Passos, David Cournapeau, Matthieu Brucher, Matthieu Perrot, and Édouard Duchesnay. Scikit-learn: Machine Learning in Python. *Journal of Machine Learning Research*, 12(85):2825–2830, 2011. URL http://jmlr.org/papers/v12/pedregosa11a.html.

[39] Simon J. Pelletier and Francesca Cicchetti. Cellular and Molecular Mechanisms of Action of Transcranial Direct Current Stimulation: Evidence from In Vitro and In Vivo Models. *International Journal of Neuropsychopharmacology*, 18(2):pyu047, January 2015. ISSN 1461-1457. doi: 10.1093/ijnp/pyu047. URL https://www.ncbi.nlm.nih.gov/pmc/articles/PMC4368894/.

[40] Oula Puonti, Koen Van Leemput, Guilherme B. Saturnino, Hartwig R. Siebner, Kristoffer H. Madsen, and Axel Thielscher. Accurate and robust whole-head segmentation from magnetic resonance images for individualized head modeling. *NeuroImage*, 219:117044, October 2020. ISSN 1053-8119. doi: 10.1016/j.neuroimage.2020.117044. URL https://www.sciencedirect.com/science/article/pii/S1053811920305309.

[41] Mark Raasveldt and Hannes Mühleisen. DuckDB: an embeddable analytical database. ACM, June 2019. doi: 10.1145/3299869.3320212. URL https://doi.org/10.1145/3299869.3320212.

[42] Thomas Radman, Raddy L. Ramos, Joshua C. Brumberg, and Marom Bikson. Role of cortical cell type and morphology in subthreshold and suprathreshold uniform electric field stimulation in vitro. *Brain Stimulation*, 2(4):215–228, 228.e1–3, October 2009. ISSN 1876-4754. doi: 10.1016/j.brs.2009.03.007.

[43] Sriharsha Ramaraju, Mohammed A. Roula, and Peter W. McCarthy. Modelling the effect of electrode displacement on transcranial direct current stimulation (tDCS). *Journal of Neural Engineering*, 15(1):016019, February 2018. ISSN 1741-2552. doi: 10.1088/1741-2552/aa8d8a.

[44] Carl Edward Rasmussen and Christopher K. I. Williams. *Gaussian processes for machine learning*. Adaptive computation and machine learning. MIT Press, Cambridge, Mass, 2006. ISBN 978-0-262-18253-9. URL http://www.gaussianprocess.org/gpml/chapters/RW.pdf. OCLC: ocm61285753.

[45] Lais B. Razza, Priscila Palumbo, Adriano H. Moffa, Andre F. Carvalho, Marco Solmi, Colleen K. Loo, and Andre Russowsky Brunoni. A systematic review and meta-analysis on the effects of transcranial direct current stimulation in depressive episodes. *Depression and Anxiety*, 37(7):594–608, 2020. ISSN 1520-6394. doi: 10.1002/da.23004. URL https://onlinelibrary.wiley.com/doi/abs/10.1002/da.23004. _eprint: https://onlinelibrary.wiley.com/doi/pdf/10.1002/da.23004.

[46] Tonya L. Rich and Bernadette T. Gillick. Electrode Placement in Transcranial Direct Current Stimulation—How Reliable Is the Determination of C3/C4? *Brain Sciences*, 9(3):69, March 2019. ISSN 2076-3425. doi: 10.3390/brainsci9030069. URL https://www.ncbi.nlm.nih.gov/pmc/articles/PMC6468365/.

[47] Chris Rorden, Hans-Otto Karnath, and Leonardo Bonilha. Improving lesion-symptom mapping. *Journal of Cognitive Neuroscience*, 19(7):1081–1088, July 2007. ISSN 0898-929X. doi: 10.1162/jocn.2007.19.7.1081.

[48] Etienne Sallard, Jaimie Lee Rohrbach, Catherine Brandner, Nicolas Place, and Jérôme Barral. Individualization of tDCS intensity according to corticospinal excitability does not improve stimulation efficacy over the primary motor cortex. *Neuroimage: Reports*, 1(3):100028, September 2021. ISSN 2666-9560. doi: 10.1016/j.ynirp.2021.100028. URL https://www.sciencedirect.com/science/article/pii/S266695602100026X.

[49] John Salvatier, Thomas V. Wiecki, and Christopher Fonnesbeck. Probabilistic programming in Python using PyMC3. *PeerJ Computer Science*, 2:e55, April 2016. ISSN 2376-5992. doi: 10.7717/peerj-cs.55. URL https://peerj.com/articles/cs-55. Publisher: PeerJ Inc.

[50] Philipp A. Schroeder, Tobias Schwippel, Ines Wolz, and Jennifer Svaldi. Meta-analysis of the effects of transcranial direct current stimulation on inhibitory control. *Brain Stimulation: Basic, Translational, and Clinical Research in Neuromodulation*, 13(5):1159–1167, September 2020. ISSN 1935-861X, 1876-4754. doi: 10.1016/j.brs.2020.05.006. URL https://www.brainstimjrnl.com/article/S1935-861X(20)30105-4/fulltext. Publisher: Elsevier.

[51] H.P. Schwan. Electrical properties of tissues and cell suspensions: mechanisms and models. In *Proceedings of 16th Annual International Conference of the IEEE Engineering in Medicine and Biology Society*, volume 1, pages A70–A71 vol.1, November 1994. doi: 10.1109/IEMBS.1994.412155.

[52] Daniel Senkowski, Rabea Sobirey, David Haslacher, and Surjo R Soekadar. Boosting working memory: uncovering the differential effects of tDCS and tACS. *Cerebral Cortex Communications*, 3(2):tgac018, April 2022. ISSN 2632-7376. doi: 10.1093/texcom/tgac018. URL https://doi.org/10.1093/texcom/tgac018.

[53] Dirson João Stein, Liciane Fernandes Medeiros, Wolnei Caumo, and Iraci LS Torres. Transcranial Direct Current Stimulation in Patients with Anxiety: Current Perspectives. *Neuropsychiatric Disease and Treatment*, 16:161–169, January 2020. ISSN 1176-6328. doi: 10.2147/NDT.S195840. URL https://www.ncbi.nlm.nih.gov/pmc/articles/PMC6969693/.

[54] Gaia Amaranta Taberna, Jessica Samogin, and Dante Mantini. Automated Head Tissue Modelling Based on Structural Magnetic Resonance Images for Electroencephalographic Source Reconstruction. *Neuroinformatics*, January 2021. ISSN 1539-2791, 1559-0089. doi: 10.1007/s12021-020-09504-5. URL http://link.springer.com/10.1007/s12021-020-09504-5.

[55] Tomoko Tanaka, Yoshikazu Isomura, Kazuto Kobayashi, Takashi Hanakawa, Satoshi Tanaka, and Manabu Honda. Electrophysiological Effects of Transcranial Direct Current Stimulation on Neural Activity in the Rat Motor Cortex. *Frontiers in Neuroscience*, 14, 2020. ISSN 1662-453X. URL https://www.frontiersin.org/article/10.3389/fnins.2020.00495.

[56] Blaz Valic, Muriel Golzio, Mojca Pavlin, Anne Schatz, Cecile Faurie, Bruno Gabriel, Justin Teissié, Marie-Pierre Rols, and Damijan Miklavcic. Effect of electric field induced transmembrane potential on spheroidal cells: theory and experiment. *European biophysics journal: EBJ*, 32(6):519–528, September 2003. ISSN 0175-7571. doi: 10.1007/s00249-003-0296-9.

[57] Pauli Virtanen, Ralf Gommers, Travis E. Oliphant, Matt Haberland, Tyler Reddy, David Cournapeau, Evgeni Burovski, Pearu Peterson, Warren Weckesser, Jonathan Bright, Stéfan J. van der Walt, Matthew Brett, Joshua Wilson, K. Jarrod Millman, Nikolay Mayorov, Andrew R. J. Nelson, Eric Jones, Robert Kern, Eric Larson, C J Carey, İlhan Polat, Yu Feng, Eric W. Moore, Jake VanderPlas, Denis Laxalde, Josef Perktold, Robert Cimrman, Ian Henriksen, E. A. Quintero, Charles R. Harris, Anne M. Archibald, Antônio H. Ribeiro, Fabian Pedregosa, Paul van Mulbregt, and SciPy 1.0 Contributors. SciPy 1.0: Fundamental Algorithms for Scientific Computing in Python. *Nature Methods*, 17:261–272, 2020. doi: 10.1038/s41592-019-0686-2.

[58] Jacob Westfall. Statistical details of the default priors in the Bambi library. *arXiv:1702.01201 [stat]*, February 2017. URL `http://arxiv.org/abs/1702.01201`. arXiv: 1702.01201.

[59] Samuel J Westwood. Null Effects on Working Memory and Verbal Fluency Tasks When Applying Anodal tDCS to the Inferior Frontal Gyrus of Healthy Participants. *Frontiers in Neuroscience*, 12:19, 2018.

[60] Sarah Wiethoff, Masashi Hamada, and John C. Rothwell. Variability in response to transcranial direct current stimulation of the motor cortex. *Brain Stimulation*, 7(3):468–475, June 2014. ISSN 1876-4754. doi: 10.1016/j.brs.2014.02.003.

[61] Eung Je Woo and Jin Keun Seo. Magnetic resonance electrical impedance tomography (MREIT) for high-resolution conductivity imaging. *Physiological Measurement*, 29(10):R1–26, October 2008. ISSN 0967-3334. doi: 10.1088/0967-3334/29/10/R01.

[62] Dongju Yang, Qiaoyi Du, Zhaoyang Huang, Liping Li, Zhang Zhang, Liping Zhang, Xin Zhao, Xuan Zhao, Ting Li, Yicong Lin, and Yuping Wang. Transcranial Direct Current Stimulation for Patients With Pharmacoresistant Epileptic Spasms: A Pilot Study. *Frontiers in Neurology*, 10, 2019. ISSN 1664-2295. URL `https://www.frontiersin.org/article/10.3389/fneur.2019.00050`.

[63] Paul A. Yushkevich, Joseph Piven, Heather Cody Hazlett, Rachel Gimpel Smith, Sean Ho, James C. Gee, and Guido Gerig. User-guided 3D active contour segmentation of anatomical structures: Significantly improved efficiency and reliability. *Neuroimage*, 31(3):1116–1128, 2006.